Voxel-wise correlation of PET/CT with multiparametric MRI and histology of the prostate using a sophisticated registration framework

Hayley M. Reynolds[1,2], Scott Williams[2,3], Price Jackson[1,2], Catherine Mitchell[4], Michael S. Hofman[2,5], Rodney J. Hicks[2,5], Declan G. Murphy[2,6], Annette Haworth[7]

[1] Department of Physical Sciences, Peter MacCallum Cancer Centre, Melbourne, Victoria 3000, Australia

[2] Sir Peter MacCallum Department of Oncology, The University of Melbourne, Melbourne, Victoria 3010, Australia

[3] Division of Radiation Oncology, Peter MacCallum Cancer Centre, Melbourne, Victoria 3000, Australia

[4] Department of Pathology, Peter MacCallum Cancer Centre, Melbourne, Victoria, Australia

[5] Cancer Imaging, Peter MacCallum Cancer Centre, Melbourne, Victoria, Australia

[6] Division of Cancer Surgery, Peter MacCallum Cancer Centre, Melbourne, Victoria, Australia

[7] School of Physics, The University of Sydney, Sydney, New South Wales, Australia

This is the author manuscript accepted for publication and has undergone full peer review but has not been through the copyediting, typesetting, pagination and proofreading process, which may lead to differences between this version and the Version of Record. Please cite this article as doi: 10.1111/bju.14648

DR. HAYLEY M REYNOLDS (Orcid ID : 0000-0001-8146-1113)

DR. DECLAN MURPHY (Orcid ID : 0000-0002-7500-5899)

Article type : Original Article

Article category: Urological Oncology

Corresponding Author Email ID: **Hayley.Reynolds@petermac.org**

ABSTRACT

Objectives

To develop a registration framework for correlating positron emission tomography/computed tomography (PET/CT) images with multiparametric MRI (mpMRI) and histology of the prostate, thereby enabling voxel-wise analysis of imaging parameters.

Patients and methods

In this prospective proof-of-concept study, nine patients scheduled for radical prostatectomy underwent mpMRI and PET/CT imaging prior to surgery. One had PET imaging using ^{18}F-fluoromethylcholine (FCH), five using ^{68}Ga-labelled prostate-specific membrane antigen (PSMA)-HBED-CC (PMSA-11) and three using a trial ^{68}Ga-labelled THP-PSMA tracer. PET/CT data was co-registered with mpMRI via the CT scan and an in vivo 3D T2w MRI, and then co-registered with ground truth histology data using ex vivo MRI of the prostate specimen. Maximum and mean standardised uptake values (SUVmax and SUVmean) were extracted from PET data using tumour annotations from histology, and Kolmogorov-Smirnov

tests were carried out to compare between tumour and benign voxel values. Correlation analysis was performed between mpMRI and PET SUV tumour voxels using Pearson's correlation coefficient and R squared statistics.

Results

PET/CT data from all nine patients were successfully registered with mpMRI and histology data. SUVmax and SUVmean ranged from 2.21 to 12.11 and 1.08 to 4.21, respectively. All patients showed the PET SUV values in benign and tumour voxels were from statistically different distributions. Correlation analysis showed no consistent trend between the T2w or ADC values and PET SUV. However, parameters from DCE MRI including the maximum enhancement (ME), volume transfer constant Ktrans and the initial area under the contrast agent concentration curve (iAUGC60) showed consistent positive correlations with PET SUV. Furthermore, R2* values from BOLD MRI showed consistent negative correlations with PET SUV voxel values.

Conclusion

We have developed a novel framework for registering and correlating PET/CT data at a voxel-level with mpMRI and histology. Despite registration uncertainties, perfusion and oxygenation parameters from DCE MRI and BOLD imaging showed correlations with PET SUV. Further analysis will be performed on a larger patient cohort to quantify these proof-of-concept findings. Improved understanding of the correlation between mpMRI and PET will provide supportive information for focal therapy planning of the prostate.

Keywords

multiparametric MRI, PET/CT, prostate cancer, image registration, focal therapy, PSMA

INTRODUCTION

Recent landmark studies have helped define the role of multiparametric magnetic resonance imaging (mpMRI) in the early detection of prostate cancer. Prospective studies have

demonstrated its value for detecting clinically significant prostate cancer (1), and also the accuracy of targeted biopsies in men with suspicious lesions on mpMRI (2). Combined, data from the PROMIS and PRECISION studies provide a compelling argument for mpMRI to be used as a triage tool for men suspected of having early prostate cancer and for targeted biopsies to be used instead of systematic biopsies (3). Furthermore, this paradigm also provides a foundation to select men for focal therapy.

Accurate implementation of biologically-guided focal therapy requires precise tumour delineation and characterisation of intra-prostatic tumour heterogeneity. Most focal therapy strategies rely on mpMRI and saturation biopsy techniques such as transperineal mapping biopsies (4), however it is accepted that mpMRI will miss a proportion of clinically significant prostate cancers (5). A promising way to augment this approach is to combine information from mpMRI with molecular information derived from positron emission tomography (PET) (6). To date, mpMRI has typically focussed on local staging while PET has focussed on detecting metastatic disease (7–9). Recent studies have shown that in combination they can provide increased sensitivity and specificity for lesion detection (10) and can improve treatment planning when compared with using one imaging modality alone (11). In particular, small but clinically significant lesions which are undetectable on mpMRI may still be visualised on PET when there is high tracer uptake, even when the lesion is below the theoretical spatial resolution of the PET scanner. Conversely, lesions close to the bladder base can be obscured by urinary activity but visualised on mpMRI.

Despite these benefits, substantial uncertainty remains regarding how to define and integrate tumour volumes from imaging into focal therapy planning. Previous focal therapy studies have used variable and subjective definitions of tumour volume, such as low ADC values from diffusion weighted imaging (DWI), and a consensus about the best approach is yet to be reached. In addition, there is a lack of knowledge about how mpMRI and PET relate to each other and only a limited number of studies with either small datasets or no access to ‘ground truth’ histology data have been carried out to quantify these relationships (12,13). While it is known that accurate quantification of prostate tumour heterogeneity in mpMRI and PET (14) needs to be assessed against histology, these data are not always readily available and it is also challenging to precisely correlate histology with imaging data (15).

To address these limitations, in this proof-of-concept study we sought to build upon our existing co-registration framework (16) to correlate prostate PET imaging and mpMRI with

ground truth histology. Our ultimate goal is to use these data to improve the sensitivity of voxel-level prediction models developed using machine learning by our research group to locate and characterise prostate tumours (17,18). This will be used in 'biofocussed radiotherapy' (BiRT) treatment planning, a novel form of focal therapy which takes intra-tumoural heterogeneity into account.

PATIENTS AND METHODS

Forty-five prostate cancer patients treated by radical prostatectomy at Peter MacCallum Cancer Centre (PMCC), Melbourne, were recruited to our Human Research Ethics Committee (HREC) approved mpMRI study and provided their written informed consent. Nine of these patients also had PET/CT imaging to assess their disease and were eligible for this study. The mpMRI and PET/CT imaging were acquired at PMCC in all but patient 6 who had their PET/CT obtained at Monash Imaging, Melbourne. Clinical and pathological details for each patient are given in Table 1. Median patient age was 65 years (interquartile range 9 years), PSA ranged from 2.2 – 42 ng/ml, PIRADS version 2 (19) of the index lesion was either 4 or 5, and Gleason Score of the index lesion was 7 (either 3+4 or 4+3) in all except patient 9 who had a Gleason Score 9 (5+4) tumour. The median number of days before radical prostatectomy that each imaging study was performed was 15 days for PET/CT and 14 days for mpMRI.

[Table 1 near here]

PET/CT imaging

Table 2 summarises the PET/CT details for each patient including the type of tracer, the injected activity, uptake time and the voxel size of the PET and CT images. As we did not have a specified study protocol for the PET imaging, three different tracers were used across the patient cohort, with patient 1 having ^{18}F-fluoromethylcholine (FCH) and the remaining patients having a ^{68}Ga-labelled prostate-specific membrane antigen (PSMA) tracer. This included patients 2 to 6 who had ^{68}Ga PSMA-HBED-CC (PMSA-11) while patients 7 to 9 had a new radiopharmaceutical tracer ^{68}Ga THP-PSMA as part of a Phase I study carried out at PMCC (20).

[Table 2 near here]

Five different PET/CT scanners were used, and patients were scanned from either the base of the skull to the upper thighs or from the vertex to the upper thighs. The contemporaneous low dose non-contrast multi-slice CT scans obtained were used for anatomic correlation and attenuation correction.

The three patients on the ^{68}Ga THP-PSMA study had a PET/CT scan at the time of injection (time = 0 minutes), and repeated PET imaging only (i.e. without a CT scan) every 15 minutes for the first 90 minutes, and then two full PET/CT acquisitions at 2 hours and 3 hours post injection. For this study we have analysed the data acquired at 2 hours post injection (see Table 2) as this gave the maximum tracer uptake in the PET images whilst ensuring there was a full CT scan obtained at the same time for accurate co-registration with MRI.

Multiparametric MRI

A dedicated mpMRI for this study was performed according to the research protocol outlined here. All patients underwent mpMRI using a 3 Tesla (3T) Siemens Trio Tim scanner (Siemens Medical Solution, Erlangen, Germany). A torso surface coil was used, without an endorectal coil in order to reduce the chance of deformation to the prostate during scanning. The protocol was based on the European Society of Urogenital Radiology (ESUR) guidelines (21), and included T2-weighted, diffusion weighted (DWI), and dynamic contrast enhanced (DCE) imaging. DWI data was acquired using an axial echo-planar imaging sequence with b values of 50, 400, 800 and 1200 s/m^2, after which apparent diffusion coefficient (ADC) maps were computed by fitting a mono-exponential decay curve to the DWI data in Siemens software.

DCE data was obtained using a 3D T1-weighted TWIST sequence with each patient receiving a 10ml bolus injection of contrast agent Dotarem (gadoterate meglumine, Guerbet, USA), followed by a saline flush. Semi-quantitative parametric maps and pharmacokinetic parameters were computed from the DCE MRI data using Dynamika software (Image Analysis Group, London, UK) (22). This included the initial rate of enhancement (IRE), the initial rate of washout (IRW), the time of contrast agent onset (T_{onset}), the time of contrast agent washout ($T_{washout}$), the maximum enhancement (ME) and the time to peak (TTP), and Ktrans, the volume transfer constant between blood plasma and the extra-vascular extra-

cellular space, computed using the Tofts model (23). The initial area under the contrast agent concentration curve for the first 60 seconds post-injection (iAUGC60) was also computed.

In addition to the standard ESUR sequences, blood oxygen level dependent (BOLD) imaging was acquired for all except patient 1. A T2* map was calculated from the raw BOLD data by fitting a mono-exponential decay curve, and the reciprocal taken to produce an R2* map. A 3D T2w image was obtained from all patients to aid the co-registration between in vivo and ex vivo MRI. The 3D T2w image for patients 1 to 3 were acquired with near isotropic voxels of 0.625 x 0.625 x 0.6 mm, while patients 4 to 9 all had 3D T2w MRI acquired with isotropic voxels of 0.8 mm. As part of the co-registration process, the prostate boundary was contoured on both in vivo and ex vivo T2w images by an experienced radiation oncologist (SW).

Radical prostatectomy

All radical prostatectomies were performed using a robotic-assisted approach as previously described (24). Lymph node dissection was performed at the surgeon's discretion. Prostate specimens were sent fresh for ex-vivo MRI prior to pathological examination.

Ex vivo MRI and histology data

After radical prostatectomy, each patient's prostate specimen was embedded in agarose gel within a custom-made sectioning box with cutting slots 5 mm apart. Two ex vivo T2w MR images were obtained: an axial T2w dataset with a high in-plane resolution of 0.22 mm and slice thickness of 2.5 mm to enable registration of every second image with histology; and an isotropic 3D T2w image to co-register with the in vivo 3D T2w MRI. Similar to the in vivo 3D T2w MRI, patients 1 to 3 were acquired with near isotropic voxels of 0.625 x 0.625 x 0.6 mm. The ex vivo 3D T2w MRI for patients 4 to 9 all had isotropic voxels of 0.8 mm. After MR imaging the prostate specimen was cut into 5 mm thick sections according to the box cutting slots. Histology sections were microtomed from the top surface of each section, stained with haemotoxylin and eosin (H&E), and tumour foci annotated with Gleason Scores by an experienced uro-pathologist (CM). Further details of this process are given in Reynolds et al. (16).

Co-registration

Co-registration of PET/CT with mpMRI and histology in this study builds upon a framework previously developed by our group to register mpMRI and histology (16), which has been slightly modified (see Figure 1) compared to its initial description so that the clinical mpMRI is co-registered directly with the in vivo 3D T2w MRI instead of the axial T2w MRI. This provides improved co-registration due to the higher resolution of the in vivo 3D T2w images compared with the axial T2w images. All final co-registered images are in the ex vivo 3D T2w image frame of reference.

[Figure 1 near here]

To register PET/CT images, the higher resolution CT images were directly registered with the 3D T2w MRI, using 3D Slicer software (25). This involved cropping and manually aligning the CT with the 3D T2w MRI using bony anatomy close to the prostate (heads of femurs and the pelvis). Automatic registration was then applied using the manually aligned CT image (the 'moving' image) with the 3D T2w image (the 'reference' image), using mutual information as the similarity metric. The PET image was co-registered using this same transformation matrix. Results were visually assessed to determine if the prostate boundary was well aligned between the CT and MRI. The location of the bladder neck frequently seen on PET was also visually compared with its location on 3D T2w MRI, and if also well aligned the registration was finalised. If the registration required improvement, the CT was cropped further to exclude bony anatomy before applying another automatic registration or making manual adjustments.

After each patient's CT had been registered with in vivo 3D T2w MRI, deformable image registration (DIR) was applied using a pre-computed transformation to the rigidly registered PET/CT images to co-register them with ex vivo MRI and histology. This required resampling the PET/CT images to the same resolution as the ex vivo 3D T2w MRI.

Statistical analysis

Voxel-wise statistical analysis of the co-registered PET/CT, mpMRI and histology data was carried out. To take registration error into account, tumour voxels from the histology annotations were dilated by 3.3 mm in-plane, based on the registration uncertainty estimated

previously between in vivo MRI and histology (16). Any voxels that fell outside the contoured prostate boundary were excluded.

Maximum and mean standardised uptake values (SUVmax and SUVmean) values from PET within the dilated tumour annotations were computed, while all voxels outside the tumour annotations were categorised as benign. Two sample Kolmogorov-Smirnov tests were performed to quantify whether the PET SUV values in tumour and benign voxels were from different distributions. Correlation analysis was conducted by computing Pearson's correlation coefficient between PET SUV and mpMRI tumour voxel values. Bonferroni correction was applied to adjust for multiple comparisons and R squared statistics were computed to quantify the scatter around the fitted regression line.

RESULTS

The PET/CT images from each patient were all successfully co-registered with the 3D T2w MRI, giving PET/CT data in the ex vivo 3D T2w MRI frame of reference along with the mpMRI and histology data. Six of the nine patients were registered using automatic registration, while patients 2, 8 and 9 required manual adjustments. Patient 2 needed a manual adjustment due to a CT image artefact, patient 8 showed the bladder neck was misaligned between PET and 3D T2w MRI after the initial automatic registration, while patient 9 had a large amount of gas in the rectum on CT not shown in the 3D T2w MRI.

An example registration is shown in Figure 2 for patient 3. The PET data is overlaid with ground truth histology and dilated tumour annotation data in Figure 2a, while the in vivo 3D T2w MRI and PET data are shown in axial, sagittal and coronal views in Figures 2b-d. Tumour annotations are shown on alternating image slices according to the sectioning method utilised, interpolated over a 2.5 m slice thickness to match with ex vivo 2D T2w MRI. The effect of non-linear warping of the in vivo 3D T2w MRI data due to DIR can be seen around the boundaries of the images. The highest PET tracer uptake is shown within the tumour, however there is also low-grade uptake shown in benign tissue.

[Figure 2 near here]

Figure 3 displays results for all patients, showing the co-registered PET images, in vivo 3D T2w MRI and the tumour annotations from histology. Most patients showed a clear overlap

between areas of high uptake on PET compared with the tumour boundaries, however patients 2, 7 and 9 showed high uptake outside the tumour. Of these, patient 2 had the largest tumour (8000 mm^3, refer Table 1), with a Gleason Score of 4+3 (ISUP grade group 3), and showed heterogeneous uptake throughout the prostate without a clear distinctive focus on PET. Patients 7 and 9 were both from the ^{68}Ga THP-PSMA study, where the PET/CT images co-registered were acquired at 2 hours post injection. Patient 7 did not have clear focal uptake within the tumour above the background signal but instead showed high uptake in the urethra which corresponded with co-registered MRI, and has therefore not been assessed in subsequent statistical analysis. Patient 9 had heterogeneous diffuse uptake in these late images which did not match the tumour location, in contrast to earlier images which showed some focal uptake in the prostatic apex corresponding with the tumour.

[Figure 3 near here]

SUVmax and SUVmean values for each patient, are given in Table 3. The highest values were 12.11 and 4.21 respectively for patient 5, who had the highest PSA of all patients at 42 ng/ml, a Gleason Score 7 (4+3) and PIRADS 4 tumour. The remaining patients had SUVmax values ranging from 2.21 to 9.64 and SUVmean values ranging from 1.08 to 3.97, with the lowest values for trial ^{68}Ga THP-PSMA patient 9.

[Table 3 near here]

Kolmogorov Smirnov tests showed all patients had tumour voxel values from significantly different distributions compared to the benign voxel values. Results from the correlation analysis are given in Table 4, detailing the Pearson's correlation coefficient ρ and R squared values between PET SUV and mpMRI tumour voxel values. There were many low R squared values shown in the results, likely due to scatter around the fitted regression line from the small voxel size of the co-registered data after registration resampling relative to the original low PET resolution.

There was no consistent pattern shown in the correlation coefficients between axial T2w MRI data and PET SUV, and very low R squared values ranging from 0.00 to 0.03. Similarly, the ADC voxel values showed a high degree of scatter and no consistent trend in correlation coefficients across all patients. The highest correlations (and R squared values) were shown in patients 1, 5 and 6 which were -0.22 (0.05), -0.44 (0.20) and -0.25 (0.06) respectively.

In contrast, excluding results from patients 8 and 9 which were statistically insignificant, DCE MRI parameters ME, Ktrans and iAUGC60 were all positively correlated with PET SUV voxel values. Pearson's ρ ranged from 0.16 to 0.70 for the ME parameter, from 0.09 to 0.70 for Ktrans, and from 0.32 to 0.67 for iAUGC60; while R squared ranged from 0.03 to 0.49 for ME, from 0.01 to 0.49 for Ktrans, and from 0.10 to 0.45 for iAUGC60. Figure 4 shows co-registered PET/CT and mpMRI maps with particularly high correlations for patient 3 and Figure 5 gives the corresponding binned scatterplots. In addition, the IRE parameter showed positive correlations for all except patients 8 and 9.

Conversely, all correlations that were statistically significant between the R2* map and PET SUV voxel values were negative, ranging from -0.06 to -0.54. However, low R squared values were shown for a number of these correlations. The number of voxels available for analysis from the R2* map was frequently lower than the other mpMRI maps, as the imaging protocol only obtained 10 slices at 4 mm slice thickness, so the entire gland was not always obtained.

[Table 4 near here]

[Figures 4 & 5 near here]

DISCUSSION

The value of mpMRI is now well established for the early detection and local staging of prostate cancer. PSMA PET is a novel modality with high tumour-to-background contrast (26,27) and there is an evolving role for staging patients with intermediate or high-risk prostate cancer (8,28). Hence, the combined use of mpMRI and PSMA PET imaging for biologically guided prostate focal therapy will provide the ultimate in precision medicine, enhancing the ability to accurately detect tumours and characterise intra-tumoural heterogeneity. With emerging evidence for the value of combined PET/MRI technology (29,30) a thorough understanding of the correlation of each imaging modality with each other and with histology is vital.

Within this proof-of-concept study we have successfully developed and implemented a method for co-registering PET/CT with mpMRI and histology by building upon our existing registration framework. Results have demonstrated the association of PET imaging with ground truth histology and given insights into the correlation of mpMRI with PET for a small cohort of patients. The particular advantage of this study is the refined registration method

and the voxel-level analysis, as only a small number of voxel-based correlation studies have been carried out previously (12,13).

Findings must be interpreted with the limitations in mind, which included the use of three different PET tracers, five different PET/CT scanners and different voxel sizes in the imaging data. ^{18}F FCH reflects increased choline transport and overexpression of choline kinase in cancer cells, and is not as sensitive as ^{68}Ga-HBED-PSMA-11 which indicates the expression of PSMA and is significantly higher in prostate cancer cells (31). Similarly, ^{68}Ga THP-PSMA has been shown to be less sensitive than ^{68}Ga-HBED-PSMA-11 with SUVmax values approximately three times lower (mean 10.7 versus mean 30.3, $p<0.01$) (20). Previous studies have shown that, in patients with a mean PSA of 10.46, an SUVmax value >= 5.4 can discriminate between clinically and non-clinically significant cancers (32). As PSA has shown to be a significant predictor of a positive PSA result (33), then clearly the ability of a PET tracer to discriminate between tumour and benign tissue will be a function of both the tracer sensitivity and a patient's PSA. In this study, we have not attempted to elucidate the relationship between tracer sensitivity and PSA, but develop a co-registration framework which could be applied in future studies to accurately address this issue. However, we acknowledge the patients scanned with the lower sensitivity tracer (^{68}Ga THP-PSMA) all had low PSA values (<=6.2) which meant analysis of data from these patients was challenging.

In addition, we did not account for the difference in sensitivities between the tracers but instead considered only the ability of the imaging methods to differentiate between tumour and benign tissue. Hence we predict that future studies which consider only the most sensitive isotopes are more likely to give reliable results. This is shown in the ^{18}F FCH patient and five ^{68}Ga-HBED-PSMA-11 patients that had consistent associations between DCE MRI data and PET uptake values. The positive correlations observed between the IRE, ME, Ktrans and iAUGC60 parameters with PET SUV may be explained by the higher level of PET uptake within tumour voxels that have a higher amount of perfusing vessels, simply because the tracer is more readily transported to those areas. Conversely, the negative correlation between R2* from BOLD imaging which is typically used to assess hypoxia may indicate that tumour voxels with lower oxygenation are more likely to have a lower PET tracer uptake.

Two different 3D T2w MRI resolutions were used, with the first three patients having a voxel volume of 0.23 mm^3 and the remaining six having voxels 0.51 mm^3. The latter enabled a

decrease in data acquisition time whilst still providing adequately resolved features for accurate co-registration. The resampling of co-registered PET data which originally had voxel volumes ranging widely from 26.7 mm^3 to 60.5 mm^3, was necessary in this registration framework. It assumed the smaller voxels adequately represented the physical uptake of the tracer in the smaller volume, and hence did not impact on the quality of the PET/CT data.

Larger validation studies are required to assess these correlations, which may indicate which mpMRI sequences give complementary or additional information to inform focal therapy. Our team has a particular interest in biologically optimised focal therapy which applies a non-uniform distribution of radiation dose in an effort to maximise tumour control and limit side effects through minimising irradiation of normal tissues. The role of PSMA PET in this scenario is to improve the overall sensitivity and specificity of a model to spatially define the biological characteristics of tumours to inform the treatment planning process (34,35). The registration framework we have developed however is generalisable and could be applied in many diagnostic and theragnostic applications (9,11,28).

Accurate registration of PET/CT with mpMRI and histology is known to be a challenging task due to differences in resolution, soft tissue contrast and partial volume effects, not to mention the deformations the prostate undergoes between each imaging study, surgery and pathological processing. A review by Meyer et al. (15) summarised the techniques used to correlate imaging with histology into four categories, and noted the most accurate was to directly register 3D prostate imaging with stacked 2D histology slices (36,37), ideally aided by ex vivo imaging of the prostate specimen. We have utilised this technique, by building upon methods described in a study by Park et al. (38). This along with subsequent studies by Park and colleagues (38–41) used ex vivo MRI of the prostate specimen and DIR to co-register PET with histology for imaging validation. Similar recent studies by Zamboglou and colleagues (42–45) have correlated PET/CT with pathology by using ex vivo CT as reference to create a 3D histology volume, from which a synthetic PET image (‘histoPET’) was created and registered with the (original) PET data. While these studies are novel, results were predetermined by assuming tumour locations in the histoPET image accurately correlated with the tumour in PET imaging, which may not be correct.

Quantifying registration accuracy between PET/CT and histology is challenging, and many studies have not reported validation metrics. Similarly, we did not perform a quantitative assessment of the registration accuracy between PET and histology as the low soft tissue

contrast in CT compared with MRI made finding definitive points of correspondence impossible. However, in order to account for registration uncertainty we applied the estimated uncertainty between MRI and histology of 3.3 mm from our prior study (16) to dilate the tumour annotations. Whilst this does not quantify the uncertainty between PET and histology directly, we expect it will compensate for the errors in the registration process.

Despite its limitations, this study provides a sophisticated framework for the co-registration of PET/CT data with mpMRI and ground truth histology and new insights into the role of PET to complement mpMRI for focal therapy treatment strategies. PET data from more patients will be co-registered using this framework in the future, to further investigate and validate these findings.

CONCLUSION

Co-registration of PET/CT imaging with mpMRI and ground truth histology was successfully carried out in all patients, building upon an existing novel registration framework which incorporates ex vivo MRI. Registration was performed between each patient's CT scan and in vivo 3D T2w MRI specifically acquired for the co-registration process, and the computed transformation applied to the corresponding PET data. Voxel-wise correlation of imaging signals from co-registered PET and mpMRI sequences was carried out, and validated using histological information. Perfusion and oxygenation parameters from DCE MRI and BOLD imaging showed correlations with PET SUV voxel values. Further analysis will be performed on a larger patient cohort to quantify these proof-of-concept findings.

Acknowledgements

Dr Reynolds is funded by a Movember Young Investigator Grant through the Prostate Cancer Foundation of Australia's (PCFA) Research Program. This study is supported by the National Health and Medical Research Council (NHMRC) grant 1126955 and a PdCCRS grant 628592 with funding partners: PCFA, and the Radiation Oncology Section of the Australian Government Department of Health and Aging and Cancer Australia. Professor Hofman is supported by a Clinical Fellowship Award from the Peter MacCallum Foundation and a Movember Clinical Trials Award awarded through the PCFA's Research Program. Professor

Hicks is supported by a National Health and Medical Research Practitioner Fellowship Grant. The authors would like to thank Courtney Savill and Lauren Caspersz for their contribution to specimen preparation and MRI acquisition, respectively.

Conflicts of Interest

Dr Reynolds reports grants from PCFA, during the conduct of the study. Professor Hofman reports personal fees from Ipsen (honorarium for lecture), Sanofi Genzyme (honorarium for lecture), Endocyte (honorarium for advisory board) outside the submitted work. Professor Hicks reports grants from NHMRC of Australia, during the conduct of the study and personal fees from Endocyte, outside the submitted work. Professor Haworth reports grants from NHMRC, PCFA, the Radiation Oncology Section of the Australian Government Department of Health and Aging, and Cancer Australia, during the conduct of the study.

References

1. Ahmed HU, El-Shater Bosaily A, Brown LC, Gabe R, Kaplan R, Parmar MK, et al. Diagnostic accuracy of multi-parametric MRI and TRUS biopsy in prostate cancer (PROMIS): a paired validating confirmatory study. Lancet. 2017;389(10071):815–22.

2. Kasivisvanathan V, Rannikko AS, Borghi M, Panebianco V, Mynderse LA, Vaarala MH, et al. MRI-Targeted or Standard Biopsy for Prostate-Cancer Diagnosis. N Engl J Med. 2018;378(19):1767–77.

3. Nzenza T, Murphy DG. PRECISION delivers on the PROMIS of mpMRI in early detection. Nat Rev Urol. 2018;

4. van den Bos W, Scheltema MJ, Siriwardana AR, Kalsbeek AMF, Thompson JE, Ting F, et al. Focal irreversible electroporation as primary treatment for localized prostate cancer. BJU Int. 2018;121(5):716–24.

5. Branger N, Maubon T, Traumann M, Thomassin-Piana J, Brandone N, Taix S, et al. Is negative multiparametric magnetic resonance imaging really able to exclude significant prostate cancer? The real-life experience. BJU Int. 2017;119(3):449–55.

6. Koo PJ, Kwak JJ, Pokharel S, Choyke PL. Novel Imaging of Prostate Cancer with MRI, MRI/US, and PET. Curr Oncol Rep. 2015;17(12):56.

7. Lindenberg L, Ahlman M, Turkbey B, Mena E, Choyke P. Advancement of MR and PET/MR in Prostate Cancer. Semin Nucl Med. Elsevier; 2016;46(6):536–43.

8. van Leeuwen PJ, Emmett L, Ho B, Delprado W, Ting F, Nguyen Q, et al. Prospective evaluation of 68Gallium-prostate-specific membrane antigen positron emission tomography/computed tomography for preoperative lymph node staging in prostate cancer. BJU Int. 2017;119(2):209–15.

9. Murphy DG, Hofman M, Lawrentschuk N, Maurer T. Bringing clarity or confusion? The role of prostate-specific membrane antigen positron-emission/computed tomography for primary staging in prostate cancer. BJU Int. 2017;119(2):194–5.

10. Eiber M, Weirich G, Holzapfel K, Souvatzoglou M, Haller B, Rauscher I, et al. Simultaneous 68Ga-PSMA HBED-CC PET/MRI Improves the Localization of Primary Prostate Cancer. Eur Urol. 2016;70(5):829–36.

11. Zamboglou C, Thomann B, Koubar K, Bronsert P, Krauss T, Rischke HC, et al. Focal dose escalation for prostate cancer using68Ga-HBED-CC PSMA PET/CT and MRI: A planning study based on histology reference. Radiat Oncol. 2018;13(1):1–9.

12. Mera Iglesias M, Aramburu Núñez D, Del Olmo Claudio JL, López Medina A, Landesa-Vázquez I, Salvador Gómez F, et al. Multimodality functional imaging in radiation therapy planning: Relationships between dynamic contrast-enhanced MRI, diffusion-weighted MRI, and 18F-FDG PET. Comput Math Methods Med. 2015;2015.

13. Eiber M, Nekolla SG, Maurer T, Weirich G, Wester HJ, Schwaiger M. 68Ga-PSMA PET/MR with multimodality image analysis for primary prostate cancer. Abdom Imaging. 2015;40(6):1769–71.

14. Asselin M, Connor JPBO, Boellaard R, Thacker NA, Jackson A. Quantifying heterogeneity in human tumours using MRI and PET. Eur J Cancer. 2012;48(4):447–55.

15. Meyer C, Ma B, Kunju LP, Davenport M, Piert M. Challenges in accurate registration of 3-D medical imaging and histopathology in primary prostate cancer. Eur J Nucl Med Mol Imaging. 2013;40(Suppl. 1):S72–8.

16. Reynolds HM, Williams S, Zhang A, Chakravorty R, Rawlinson D, Ong CS, et al.

Development of a registration framework to validate MRI with histology for prostate focal therapy. Med Phys. 2015;42(12).

17. Sun Y, Reynolds H, Wraith D, Williams S, Finnegan ME, Mitchell C, et al. Predicting prostate tumour location from multiparametric MRI using Gaussian kernel support vector machines: a preliminary study. Australas Phys Eng Sci Med. 2017;40(1):39–49.

18. Sun Y, Reynolds HM, Wraith D, Williams S, Finnegan ME, Mitchell C, et al. Voxel-wise prostate cell density prediction using multiparametric magnetic resonance imaging and machine learning. Acta Oncol (Madr). 2018 Apr;

19. Weinreb JC, Barentsz JO, Choyke PL, Cornud F, Haider MA, Macura KJ, et al. PI-RADS Prostate Imaging - Reporting and Data System: 2015, Version 2. Eur Urol. 2016;69(1):16–40.

20. Hofman MS, Eu P, Jackson P, Hong E, Binns D, Iravani A, et al. Cold Kit PSMA PET Imaging: Phase I study of 68 Ga-THP-PSMA PET/CT in patients with prostate cancer. J Nucl Med. 2018;59(4):625–31.

21. Barentsz JO, Richenberg J, Clements R, Choyke P, Verma S, Villeirs G, et al. ESUR prostate MR guidelines 2012. Eur Radiol. 2012 Apr;22(4):746–57.

22. "Dynamika." Image Analysis Group, London, UK. http://www.ia-grp.com

23. Tofts PS, Brix G, Buckley DL, Evelhoch JL, Henderson E, Knopp M V, et al. Estimating kinetic parameters from DCE T1w MRI of a Diffusable Tracer: Standardized Quantities and Symbols. J Magn Reson imaging. 1999;10:223–32.

24. Murphy DG, Kerger M, Crowe H, Peters JS, Costello AJ. Operative Details and Oncological and Functional Outcome of Robotic-Assisted Laparoscopic Radical Prostatectomy: 400 Cases with a Minimum of 12 Months Follow-up. Eur Urol. 2009;55(6):1358–67.

25. Fedorov A, Beichel R, Kalpathy-Cramer J, Finet J, Fillion-Robin J-C, Pujol S, et al. 3D Slicer as an Image Computing Platform for the Quantitative Imaging Network. Magn Reson Imaging. 2012;30(9):1323–41.

26. Hofman MS, Hicks RJ, Maurer T, Eiber M. Prostate-specific Membrane Antigen PET: Clinical Utility in Prostate Cancer, Normal Patterns, Pearls, and Pitfalls.

Radiographics. 2018;38(1):200–17.

27. Eiber M, Fendler WP, Rowe SP, Calais J, Hofman MS, Maurer T, et al. Prostate-Specific Membrane Antigen Ligands for Imaging and Therapy. J Nucl Med. 2017;58(Supplement 2):67S–76S.

28. Hofman MS, Murphy DG, Williams SG, Nzenza T, Herschtal A, Lourenco RDA, et al. A prospective randomized multicentre study of the impact of gallium-68 prostate-specific membrane antigen (PSMA) PET/CT imaging for staging high-risk prostate cancer prior to curative-intent surgery or radiotherapy (proPSMA study): clinical trial protocol. BJU Int. 2018;(May 3).

29. Ramalho M, AlObaidy M, Catalano OA, Guimaraes AR, Salvatore M, Semelk RC. MR-PET of the body: Early experience and insights. Eur J Radiol Open. 2014;1(1):28–39.

30. Vandenberghe S, Marsden PK. PET-MRI: a review of challenges and solutions in the development of integrated multimodality imaging. Phys Med Biol. 2015;60(4):R115-54.

31. Morigi JJ, Stricker PD, van Leeuwen PJ, Tang R, Ho B, Nguyen Q, et al. Prospective Comparison of 18F-Fluoromethylcholine Versus 68Ga-PSMA PET/CT in Prostate Cancer Patients Who Have Rising PSA After Curative Treatment and Are Being Considered for Targeted Therapy. J Nucl Med. 2015;56(8):1185–90.

32. Lopci E, Saita A, Lazzeri M, Lughezzani G, Colombo P, Buffi NM, et al. 68 Ga-PSMA PET/CT for primary diagnosis of prostate cancer in men with contraindications to or negative mpMRI: a prospective observational study. J Urol. 2018;59:1–2.

33. Afshar-Oromieh A, Avtzi E, Giesel FL, Holland-Letz T, Linhart HG, Eder M, et al. The diagnostic value of PET/CT imaging with the 68Ga-labelled PSMA ligand HBED-CC in the diagnosis of recurrent prostate cancer. Eur J Nucl Med Mol Imaging. 2014;42(2):197–209.

34. Haworth A, Sun Y, Ebert M, Reynolds H, Betts J, Wraith D, et al. Incorporating a novel radiomics framework for Biologically optimised Prostate RadioTherapy (BiRT). In: Medical physics. Wiley; 2018. p. E446–E446.

35. Haworth A, Williams S. Focal therapy for prostate cancer: the technical challenges. J Contemp Brachytherapy. 2017;9(4):383–9.

36. Chang JH, Joon DL, Lee ST, Gong SJ, Scott AM, Davis ID, et al. Histopathological correlation of (11)C-choline PET scans for target volume definition in radical prostate radiotherapy. Radiother Oncol. 2011 May;99(2):187–92.

37. Mena E, Turkbey B, Mani H, Adler S, Valera VA, Bernardo M, et al. 11C-Acetate PET/CT in localized prostate cancer: a study with MRI and histopathologic correlation. J Nucl Med. 2012 Apr;53(4):538–45.

38. Park H, Piert MR, Khan A, Shah R, Hussain H, Siddiqui J, et al. Registration Methodology for Histological Sections and In Vivo Imaging of Human Prostate. Acad Radiol. 2008;15(8):1027–39.

39. Piert M, Park H, Khan A, Siddiqui J, Hussain H, Chenevert T, et al. Detection of aggressive primary prostate cancer with 11C-choline PET/CT using multimodality fusion techniques. J Nucl Med. 2009 Oct;50(10):1585–93.

40. Park H, Meyer CR, Wood D, Khan A, Shah R, Hussain H, et al. Validation of automatic target volume definition as demonstrated for 11 C-Choline PET/CT of human prostate cancer using multi- modality fusion techniques. Acad Radiol. 2011;17(5):614–23.

41. Park H, Wood D, Hussain H, Meyer CR, Shah RB, Johnson TD, et al. Introducing parametric fusion PET/MRI of primary prostate cancer. J Nucl Med. 2012 Apr;53(4):546–51.

42. Zamboglou C, Schiller F, Fechter T, Wieser G, Jilg CA, Chirindel A, et al. 68Ga-HBED-CC-PSMA PET/CT versus histopathology in primary localized prostate cancer: A voxel-wise comparison. Theranostics. 2016;6(10):1619–28.

43. Zamboglou C, Wieser G, Hennies S, Rempel I, Kirste S, Soschynski M, et al. MRI versus 68Ga-PSMA PET/CT for gross tumour volume delineation in radiation treatment planning of primary prostate cancer. Eur J Nucl Med Mol Imaging. 2016;43(5):889–97.

44. Schiller F, Fechter T, Zamboglou C, Chirindel A, Salman N, Jilg CA, et al.

Comparison of PET/CT and whole-mount histopathology sections of the human prostate: a new strategy for voxel-wise evaluation. EJNMMI Phys. 2017;4(1):21.

45. Zamboglou C, Drendel V, Jilg CA, Rischke HC, Beck TI, Schultze-Seemann W, et al. Comparison of 68Ga-HBED-CC PSMA-PET/CT and multiparametric MRI for gross tumour volume detection in patients with primary prostate cancer based on slice by slice comparison with histopathology. Theranostics. 2017;7(1):228–37.

46. Chen ME, Johnston D, Reyes AO, Soto CP, Babaian RJ, Troncoso P. A streamlined three-dimensional volume estimation method accurately classifies prostate tumors by volume. Am J Surg Pathol. 2003;27(10):1291–301.

FIGURES

Figure 1: Diagram showing how mpMRI and PET/CT data are co-registered with ex vivo MRI and histology. DIR = deformable image registration.

Figure 2: Example co-registered data for patient 3 showing (a) a 2D histology slice with tumour annotation drawn overlaid with PET, and (b-d) axial, sagittal and coronal views (respectively) showing PET, in vivo 3D T2w MRI and tumour annotations from histology.

Figure 3: Co-registered PET, in vivo 3D T2w MRI and tumour annotations for each patient numbered left to right, top to bottom.

Figure 4: Ground truth histology data with original tumour annotations, alongside co-registered PET/CT, selected mpMRI data and dilated tumour annotations for patient 3.

Figure 5: Binned scatterplots displaying PET/CT versus co-registered mpMRI voxel values for patient 3 from: (a) T2w MRI, (b) ADC maps, (c) R2* maps, and DCE maps (d) ME, (e) Ktrans and (f) iAUGC60.

Table 1: Patient clinical and pathological details. Tumour volume calculated using Chen's method (46). GS = Gleason Score.

Patient	Age	Weight (kg)	PSA (ng/ml)	Prostate weight (g)	Tumour volume (mm^3)	Pathological T-stage	GS (index lesion)	GS (other foci)	PIRADS v2 index lesion
1	59	99	6	42	7480	T2c	7 (3+4)	-	4
2	61	103	6.8	62	8000	T3b	7 (4+3)	4+4	5
3	59	68	16	50	6000	T3a	7 (4+3)	-	5
4	58	82	9	46	4000	T3b N0	9 (5+4)	5+4, 4+4, 3+4, 3+3	4
5	68	85	42	67	4500 +<1000	T3a	7 (4+3)	3+4, 3+3	4
6	70	89	8.1	41	3900	T3a N0	7 (3+4)	3+3	5
7	65	93	6.2	44	1920	T2c	7 (3+4)	3+3	5
8	66	71	5	113	4500	T2c Nx	7 (3+4)	3+4, 3+3	4
9	72	63	2.2	34	2600	T3a	7 (4+3)	3+4, 3+3	5

Table 2: PET/CT imaging details for each patient.

Patient	Tracer	PET/CT scanner	PET voxel size (mm)	CT voxel size (mm)	Injected activity (MBq)	PET uptake time (mins)
1	^{18}F-FCH	GE Stella	4.30 x 4.30 x 3.27	0.98 x 0.98 x 3.27	295	13
2	^{68}Ga PSMA-11	GE 690	2.86 x 2.86 x 3.27	1.07 x 1.07 x 3.27	118	32
3	^{68}Ga PSMA-11	GE 690	2.86 x 2.86 x 3.27	1.07 x 1.07 x 3.27	98	60
4	^{68}Ga PSMA-11	Siemens Biograph 64	3.93 x 3.93 x 3.0	1.07 x 1.07 x 3.0	105	54
5	^{68}Ga PSMA-11	Siemens Biograph 64	3.93 x 3.93 x 3.0	1.07 x 1.07 x 3.0	128	50
6	^{68}Ga PSMA-11	Siemens Biograph 16	4.07 x 4.07 x 3.0	0.98 x 0.98 x 2.0	146	72
7	^{68}Ga THP-PSMA	GE 690	2.86 x 2.86 x 3.27	1.07 x 1.07 x 3.27	228	149
8	^{68}Ga THP-PSMA	GE 690	2.86 x 2.86 x 3.27	1.07 x 1.07 x 3.27	221	123
9	^{68}Ga THP-PSMA	GE 690	2.86 x 2.86 x 3.27	1.07 x 1.07 x 3.27	241	141

Table 3: PET SUVmax and SUVmean values using tumour annotations from histology, excluding patient 7 who had no clear PET tracer uptake within the tumour.

Patients	SUVmax	SUVmean
1	8.19	3.44
2	3.88	1.89
3	6.47	3.28
4	9.64	3.97
5	12.11	4.21
6	3.70	2.25
8	5.07	2.13
9	2.21	1.08

Table 4: Pearson's correlation coefficients (R squared values in brackets), between PET SUV and mpMRI tumour voxel values, excluding patient 7 who had no clear PET tracer uptake within the tumour. Insignificant correlations are shown in bold.

	1	2	3	4	5	6	8	9
T2w	-0.02 (0.00)	0.11 (0.01)	**0.02** (0.00)	-0.05 (0.00)	-0.04 (0.00)	-0.12 (0.02)	**0.05** (0.00)	-0.17 (0.03)
ADC	-0.22 (0.05)	0.21 (0.05)	-0.03 (0.00)	0.06 (0.00)	-0.44 (0.20)	-0.25 (0.06)	0.23 (0.05)	0.10 (0.01)
IRE	0.52 (0.27)	0.33 (0.11)	0.64 (0.40)	0.17 (0.03)	0.62 (0.39)	0.39 (0.15)	-0.07 (0.01)	-0.08 (0.01)
IRW	0.04 (0.00)	0.26 (0.07)	0.31 (0.10)	-0.01 (0.00)	0.14 (0.02)	**0.02** (0.00)	0.15 (0.02)	-0.09 (0.01)
Tonset	0.31 (0.09)	0.35 (0.12)	0.39 (0.15)	-0.06 (0.00)	0.50 (0.25)	0.27 (0.07)	-0.10 (0.01)	0.07 (0.01)
Twashout	0.08 (0.01)	0.27 (0.07)	-0.09 (0.01)	-0.11 (0.01)	0.26 (0.07)	**0.00** (0.00)	0.07 (0.00)	**-0.01** (0.00)
ME	0.29 (0.09)	0.45 (0.20)	0.70 (0.49)	0.16 (0.03)	0.60 (0.36)	0.42 (0.17)	0.28 (0.08)	**0.04** (0.00)
TTP	-0.43 (0.19)	-0.07 (0.00)	-0.48 (0.23)	-0.08 (0.01)	-0.61 (0.37)	-0.33 (0.11)	0.30 (0.09)	-0.08 (0.01)
Ktrans	0.42 (0.18)	0.30 (0.09)	0.64 (0.41)	0.23 (0.05)	0.70 (0.49)	0.44 (0.20)	0.09 (0.01)	**0.02** (0.00)
iAUGC60	0.37 (0.14)	0.35 (0.12)	0.67 (0.45)	0.32 (0.10)	0.66 (0.44)	0.42 (0.18)	**0.03** (0.00)	**0.00** (0.00)
R2*		-0.12 (0.02)	-0.47 (0.22)	-0.36 (0.13)	-0.15 (0.02)	-0.06 (0.00)	-0.54 (0.29)	**0.05** (0.00)

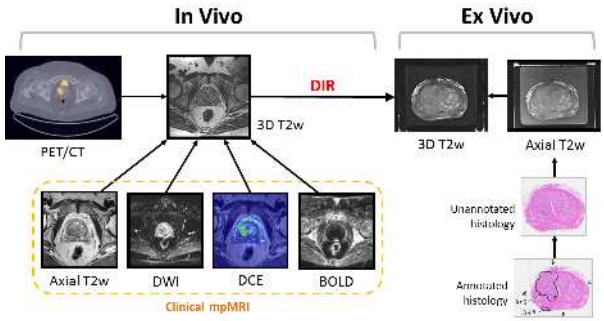

bju_14648_f1.png

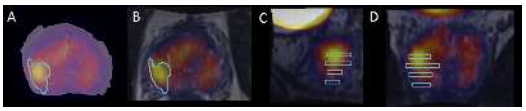

bju_14648_f2.png

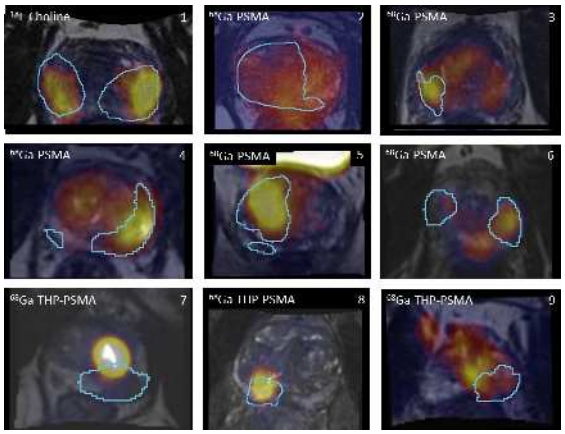

bju_14648_f3.png

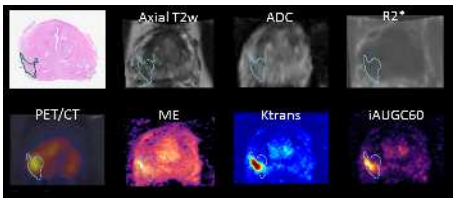

bju_14648_f4.png

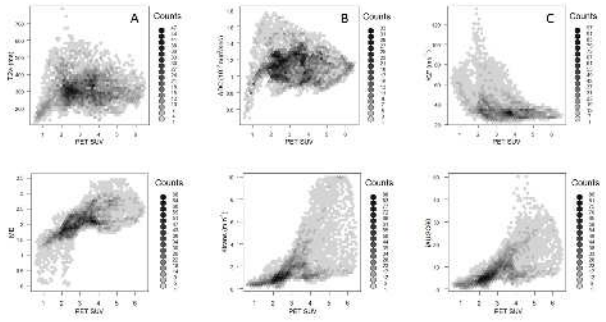

bju_14648_f5.png